ChemPlusChem

Research Article
doi.org/10.1002/cplu.202300785

Chemistry Europe
European Chemical Societies Publishing

www.chempluschem.org

Utilizing Carbonaceous Materials Derived from [BMIM][TCM] Ionic Liquid Precursor: Dual Role as Catalysts for Oxygen Reduction Reaction and Adsorbents for Aromatics and CO_2

Ourania Tzialla,[a] George V. Theodorakopoulos,*[b, c] Konstantinos G. Beltsios,[b] George Pilatos,[c] K. Suresh Kumar Reddy,[d] Chandrasekar Srinivasakannan,[e] Giulia Tuci,[f] Giuliano Giambastiani,[f, g] Georgios N. Karanikolos,[h, i] Fotios K. Katsaros,[c] Evangelos Kouvelos,[c] and George Em. Romanos*[c]

This work presents the synthesis of N-doped nanoporous carbon materials using the Ionic Liquid (IL) 1-butyl-3-methyl-imidazolium tricyanomethanide [BMIM][TCM] as a fluidic carbon precursor, employing two carbonization pathways: templated precursor and pyrolysis/activation. Operando monitoring of mass loss during pyrolytic and activation treatments provides insights into chemical processes, including IL decomposition, polycondensation reactions and pore formation. Comparatively low mass reduction rates were observed at all stages. Heat treatments indicated stable pore size and increasing volume/surface area over time. The resulting N-doped carbon structures were evaluated as electrocatalysts for the oxygen reduction reaction (ORR) and adsorbents for gases and organic vapors. Materials from the templated precursor pathway exhibited high electrocatalytic performance in ORR, analyzed using Rotating Ring-Disk electrode (RRDE). Enhanced adsorption of m-xylene was attributed to wide micropores, while satisfactory CO_2 adsorption efficiency was linked to specific morphological features and a relatively high content of N-sites within the C-networks. This research contributes valuable insights into the synthesis and applications of N-doped nanoporous carbon materials, highlighting their potential in electrocatalysis and adsorption processes.

Introduction

In recent years, porous carbons, especially nanoporous and nanostructured carbons, including Activated Carbons (AC), Carbon Nanotubes (CNTs), Carbon Aerogels (CAs), etc., have been standardized in many technological applications and become a hot scientific topic, due to their unique properties such as their high thermal and mechanical stability, electric conductivity, microwave absorption capacity, catalytic activity, tunable surface chemistry, enhanced and tailorable pore structure and wide availability.[1–2]

Electrochemistry is among the scientific fields where nanoporous carbons are gaining a steadily state interest. In particular, nanoporous carbons are considered as promising

[a] Dr. O. Tzialla
Department of Materials Science and Engineering,
University of Ioannina,
45110 Ioannina, Greece

[b] G. V. Theodorakopoulos, Prof. K. G. Beltsios
School of Chemical Engineering,
National Technical University of Athens,
Zografou Campus, 9, Iroon Polytechniou Str.,
Athens, Zografou, 15780, Greece

[c] G. V. Theodorakopoulos, Dr. G. Pilatos, Dr. F. K. Katsaros, Dr. E. Kouvelos, Dr. G. E. Romanos
Institute of Nanoscience and Nanotechnology, N.C.S.R. "Demokritos",
Ag. Paraskevi, Athens, 15310, Greece
E-mail: g.theodorakopoulos@inn.demokritos.gr
g.romanos@inn.demokritos.gr

[d] Dr. K. S. K. Reddy
Renewable and Sustainable Energy Research Center,
Technology Innovation Institute (TII),
P.O. Box 9639, Masdar City, Abu Dhabi, United Arab Emirates

[e] Prof. C. Srinivasakannan
Department of Chemical Engineering, Khalifa University,
Abu Dhabi 127788, United Arab Emirates

[f] Dr. G. Tuci, Dr. G. Giambastiani
Institute of Chemistry of OrganoMetallic Compounds, ICCOM-CNR and Consorzio INSTM, Via Madonna del Piano, 10 – 50019, Sesto F. no,
Florence, Italy

[g] Dr. G. Giambastiani
University of Florence, Department of Chemistry U. "Schiff" - DICUS – and INSTM Research Unit, Via della Lastruccia 3-13, 50019 Sesto Fiorentino (FI),
Italy

[h] Prof. G. N. Karanikolos
Department of Chemical Engineering, University of Patras,
Patras, 26504, Greece

[i] Prof. G. N. Karanikolos
Institute of Chemical Engineering Sciences,
Foundation for Research and Technology-Hellas (FORTH/ICE-HT),
26504 Patras, Greece

alternative materials to replace noble metal electrocatalysts in many applications spanning from energy conversion, batteries, storage devices, renewable energy technologies, etc.[3] even if there are still many cases, where hetero-doped nanoporous carbons are employed as simple "carriers" for a noble metal active phase.[4] Nonetheless, heteroatoms in carbon nanostructures often hold a non-innocent role with respect to the properties and stability of the ultimate composites. Heteroelements are often invoked to drive metal nanoparticles nucleation and immobilize them other than preventing undesired leaching and sintering phenomena.[5–8] In addition, doped carbons have also proven intriguing electrocatalytic activity when used as metal-free systems, particularly in the activation/conversion of small molecules.[9] Recent findings in the area of metal-free catalysis have unambiguously outlined the key role played by the heteroelement doping in C-nanostructures for the generation of structurally defective and high-energy C-active sites suitable to interact with selected molecules for their activation/conversion.

One of the most common heterodopant in carbon nanomaterials is certainly oxygen. A great variety of oxygen functional groups populate the carbon surface and all main structural vacancies formed during the material work-up or its activation step. Yet, the incorporation of other light heteroatoms, such as nitrogen, boron, and phosphorus are also known to improve the surface chemistry of these nanostructures, endowing them with greater oxidative stability, electrical conductivity, basicity, etc., other than offering improved electrocatalytic efficiency.[10–13] It is generally claimed that the introduction of heteroelement in the honeycomb C-structure, breaks the material electroneutrality and creates high-energy and structurally defective C-sites responsible for the enhanced (electro)catalytic activity of these metal-free nanomaterials. N-doped C-nanomaterials are likely the most widely used metal-free catalysts for a number of industrially relevant transformations. In spite of a number of seminal reports appeared in the last few years, the role of N-doping and the mechanism of action of these catalytic systems still remains a matter of debate within the catalysis and material science community. Both N-content, N-configuration and in-plane vs. edge position of the heterodopant are invoked time to time as responsible for the improved catalytic performance of a given sample. How the role of dopant and its loading intertwine with the morphological properties of the sample (specific surface area, pore size and pore size distribution) is still a controversial matter and a hot topic of heterogeneous catalysis promoted by metal-free systems.

Ionic Liquids (ILs) are lately considered amongst the most effective precursors for the preparation of nanostructured carbons, because they do not decompose completely into volatiles under pyrolysis but leave behind significant amounts of recalcitrant char. Moreover, there is a great variety of different IL structures that contain nitrile functional groups (–C≡N), either in the form of anion or cation,[14] thus yielding highly nitrogen-rich carbon samples.[15] Particularly, ILs can provide C-nanomaterials with a N-content even exceeding 10 wt%.[10,16] Noteworthy, this high N-loading can be achieved without any post-synthetic process like those frequently applied in combination with other C-sources. The crucial step of thermolytic process starts at 300 °C, where cyano moieties undergo trimerization reaction to give triazines, which act as stable cross-linkers and allow to preserve a high amount of carbon even at temperatures where carbonization takes place.[15] As such, ILs do not require any stabilization step to preserve the yield of carbon in the pyrolyzed product.[17] In addition, the trimerization mechanism combined with the negligible vapor pressure of ILs avoid polluting phenomena coming up during pyrolysis such as distillation, sublimation of reagents including formation of volatile intermediates.[15] ILs based on alkyl-methylimidazolium cation remain however quite expensive to be used as carbon precursors since their synthesis involves a step of alkylation reaction followed by a metathesis reaction. The exothermic character of alkylation requires high dilution and this leads to solvent expense and low production rates. Purification stages are also highly energy consuming and have significant impact to the cost. Alternatively, there are many types of cheap and easy to prepare ILs, such as aniline-based and amine-based Bronsted Acidic ILs (BAILs) that possess plenty of N atoms and could be examined as precursors for the development of N-doped carbons.[18–21] In this work, however, the 1-butyl-3-methylimidazolium tricyanomethanide [BMIM][TCM] IL was chosen due to its polycondensable anion and low viscosity. Compared to BAILs, 1-butyl-3-methylimidazolium tricyanomethanide does not have the tendency to form hydrogen bonds, resulting in significantly lower viscosity. This facilitates its imbibition into the narrow pores of porous glass. In addition, cyano-moieties in the anion undergo a trimerization reaction towards triazines, which operate as highly stable crosslinks at intermediate temperatures, leading to high carbon yields. It must be also noted that the use of ILs for the development of porous nanocarbons does not require to meet the same standards of purity as it is generally needed, when ILs (as such) are used in more advanced applications such as for gas and liquid separation or as solvents in electrochemical processes.[22–24] The high purity of ILs, that is also associated to their higher production cost, is not perceived as a critical parameter in the carbonization process to produce high-quality nanostructured C-materials.[25] It is also prosperous that lately, companies that produce ILs have invented methods based on continuous flow microreactors to perform the synthesis of alkyl-methylimidazolium based ILs, which reduce hot spots and minimize the use of solvents leading to enhanced yields at the lower energy and solvent expense. These novel approaches are expected to significantly reduce the cost of production.[26]

In a recent contribution from our team, we showed that C,N networks produced from [BMIM][TCM] exhibited significant yield in terms of N-rich nanoporous carbons with an over 20 wt% of N-content.[25] Moreover, the C,N network shown inherent microporosity and template-induced mesoporosity,[25] with slit-like micropores created spontaneously upon temperature increase without the need of any porogen or structure directing species but with a structural/templating control attributed to the non-functionalized cations.[25] Extensive porosity has a great impact in electrocatalytic reactions such as ORR,

because the higher the pore volume and the specific area, the higher the number of active sites for the process to occur.[4] Recent years have witnessed a great interest towards the preparation of carbonaceous materials by the "template" method. This approach paves the way to the production of hierarchical porous carbons (HPCs) featured by a multimodal pore size distribution of micro-, meso-, and/or macropores, a fundamental asset to get highly accessible electrochemically active sites, while reducing the diffusion distance and enhancing the mass transfer rate. Accordingly, porous carbon structures prepared by template method are found to be good candidates as effective adsorbents and/or electrocatalysts.[4]

The presence of a relatively high extent of N-containing functional groups finally affects the adsorption efficiency of these porous materials. Specifically, it increases the basic properties of the material surface that reflect its adsorption capacity and selectivity.[16,27–30] It should be mentioned that the adsorption efficiency of these materials often originates from the amount and type of active adsorption sites rather than from the structural features of the adsorbent. Especially, an extensive microporosity can be detrimental for the adsorption of large organic molecules due to mere steric effects. Therefore, for adsorption purposes, N-doped carbons with hierarchical porous structures are the preferred choice.[31] Aimed at showcasing the potentiality of [BMIM][TCM] to pyrolytically derive effective N,C-based adsorbents for model gaseous molecules (i.e., m-xylene vapors and CO_2), we also prepared - for the sake of comparison - N-doped carbons from an unconfined IL phase and we studied their adsorption efficiency.

This work is primarily focused on the investigation of the catalytic and adsorption performance of carbon materials developed through the template method. To this end, various types of enhanced pore size Vycor® (hereafter referred to eps-Vycor®) have been employed as hard templates/molds in the nanocasting/pyrolytic treatment of [BMIM][TCM] as IL precursor. Upon dissolution of the hard template, the recovered N-doped porous carbons have extensively been characterized by bimodal micro-mesoporosity.[25] Afterwards, C,N-networks prepared by this method have successfully been studied as ORR electrocatalysts showing a prevalent $4e^-$ reduction process at work and as adsorbents for m-xylene and CO_2.

Materials and Methods

Chemicals and Materials

The IL used in this work was the 1-butyl-3-methylimidazolium tricyanomethanide ([BMIM][TCM]), a relatively low viscosity IL that belongs to the class of Room Temperature Ionic Liquids (RTILs), which are the most widespread ILs in the scientific and industrial sectors because they are in the liquid state even at room temperature.[32–33] In addition, their low viscosity facilitates the imbibition of narrow pores. One main advantage of [BMIM][TCM] belongs from the presence of a N-containing cation and anion that make it an ideal precursor for developing nitrogen-rich carbonaceous samples.[34–35]

[BMIM][TCM] was provided by IoLiTech GmbH with a purity over 98% and a moisture contamination of 150 ppm. The density and dynamic viscosity at 298.15 K were respectively 1.0472 g cm^{-3} and 26.502 mPa s.[25]

Vycor® glass tube (Code 7913, Corning® USA) featured by the below mentioned structural and physical properties, was selected as the hard template for the preparation of the nanostructured carbons. Its main characteristics are summarized as follows: nominal ØD: 7 mm; nominal width: 1 mm; density: 2.18 g cm^{-3}, specific surface area: 200 m^2 g^{-1}, pore size: 4–20 nm and Young modulus: 6.62×10^{10} Pa. Other materials/chemicals (i.e., hydrogen peroxide (H_2O_2 30% (w/v)) from Panreac, ammonium difluoride (NH_4HF_2 $\geq$95% (w/w)) from Sigma-Aldrich and hydrofluoric acid (HF 40% (w/w)) from Merck were purchased and used - otherwise stated - as received.

Preparation of Enhanced Pore Vycor® Samples

Samples of pristine Vycor® tubes were purified according to the Corning® protocol. In a typical procedure, samples were heated up to 700 °C in air flow (250 mL min^{-1}), with a ramp rate of 10 °C min^{-1} and then maintained under isothermal conditions (700 °C) for 3 h. Afterwards, samples were cooled down to room temperature with a cooling rate of 10 °C min^{-1} in air flow (250 mL min^{-1}). In a next step they were soaked in a H_2O_2 30% (w/v) solution at 95 °C for half an hour before being thoroughly rinsed with deionized water. The purified pristine Vycor® samples were then stored in deionized water until use.

To enhance the pores of Vycor®, purified samples were subjected to a controlled chemical attack as described in the "Chapman and Elmer" method.[36] At first, samples were immersed in an aqueous ammonium difluoride (NH_4HF_2) solution (10% in water) for one hour and soaked in turn in nitric acid HNO_3 (1 N) at 95 °C for different times. Nitric acid promotes the generation of hydrofluoric acid (HF) inside the pores of Vycor®, leading to their widening. The samples prepared at different soaking times in nitric acid were named as follows: 2HF-Vycor®, 3HF-Vycor®, 5HF-Vycor® and 7HF-Vycor® for Vycor® tubes obtained after 2, 3, 5 and 7 hours, respectively, in HNO_3. Afterwards, the samples were carefully washed several times with ultrapure deionized water and stored in it.

Fabrication of Nanostructured Carbons from Carbon/Vycor® Composites

Nanostructured carbon syntheses via templated precursor pathway include the casting of [BMIM][TCM] into eps-Vycor® under vacuum, to facilitate the imbibition of the IL phase into the porous structure, followed by carbonization and template dissolution to recover the carbonaceous samples as eps-Vycor® replica.

The IL casting was realized under high vacuum in a specially designed cell to allow the generation of a bubble-free solid/liquid interface thus avoiding cavitation phenomena that usually unfold in the presence of gas molecules monolayers

adsorbed on the solid surface. Purified and pore enhanced Vycor® templates were firstly degassed under vacuum (10^{-3} mbar) at 140 °C for 24 h. Then the temperature was increased up to 160 °C under high vacuum conditions (10^{-3} mbar) to activate and dry adsorption sites (–OH) at the solid surface for 24 h. The procedure and conditions of activation were those suggested in the activation protocol of Corning®.

After cooling the mold down to ambient conditions, the IL was charged upon suction till filling out the solid template with the carbonaceous precursor. Afterwards, the system remained several days under vacuum, to allow a proper pore/surface wetting/imbibition of the template.

The prepared samples were then introduced in a tubular furnace (Figure 1) for pyrolysis equipped with a PID controller thermocouple for the temperature monitoring and an analytical microbalance. Samples were firstly maintained under a constant stream of Ar for several minutes (150 mL min^{-1}), before increasing the temperature up to 800 °C at a temperature rate of 10 °C min^{-1}, where all samples were kept under dynamic Ar atmosphere for 2 h.

All cooled samples were then immersed for 3 h in hydrofluoric acid (HF) to dissolve the Vycor® templates and recover the carbonaceous materials. The latter were then thoroughly washed several times with deionized water and recovered upon centrifugation. The washing procedure was continued till neutralization of the liquid phases (pH $\geq$ 5). In a very last step, solids samples were dissolved in ethanol and re-precipitated upon solvent evaporation.

The carbonization/activation process of the unconfined IL was carried out using the same pyrolysis setup and workup procedure except for using a ceramic pan for containing the IL and keeping the samples under N_2 atmosphere (100 mL min^{-1}) throughout the whole pyrolysis procedure. Samples activation was accomplished by switching the gas flow from N_2 to CO_2 (100 mL min^{-1}) when the samples temperature reached 800 °C. We applied two procedures for the activation of carbon nanostructures. The first one involved two sequential pyrolysis/activation treatments, with a total activation time of 4 h, while the second proceeded with one cycle of pyrolytic/activation treatment and a longer activation period of 8 h. All carbonization experiments applied in this work were empowered with the capacity of online monitoring and logging the mass change of the samples (Figure 1).

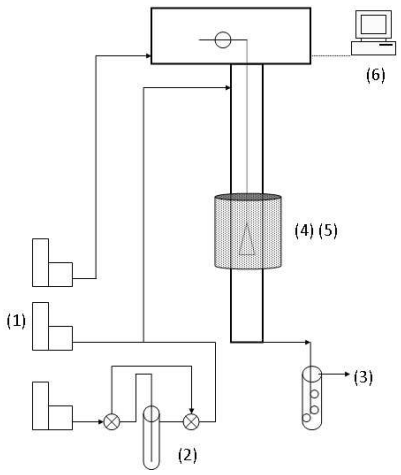

Figure 1. Pyrolysis/mass recording device employed for the pyrolysis/activation process of confined and unconfined IL. (1) mass flow controllers; (2) pressure gauge; (3) wet scrubber; (4) ceramic capsule; (5) heat zone; (6) microbalance head and data logger.

Orr Measurements

Electrochemical measurements were carried out with a Rotating Ring Disk Electrode (RRDE working electrode, Pine Instrument Co) made of a disk of glassy carbon (GC, Ø 5 mm, A = 0.196 cm^2) and a platinum (Pt) ring with a surface of 0.11 cm^2. All carbonaceous samples produced were fabricated as RRDE electrodes and measurements were performed in a three-electrode cell operating in a 0.1 M KOH solution, equipped with an [Ag][AgCl][KCl_{sat}] reference electrode and a Pt wire as counter electrode. All measurements were operated at 800 rpm under O_2 saturated atmosphere. Electrocatalysts performance was compared with that of a platinum (Pt) disc electrode (Methrom, Ø 3 mm) and each data reported as the mean value of four independent runs. Linear Sweep voltammetries (LSV) were conducted in the −1.1 to +0.2 V range vs. [Ag][AgCl][KCl_{sat}] (non-equilibrium conditions) with a scan rate of 5 mV/s. The amount of H_2O_2 produced was derived from the corresponding current density values measured at the Pt disk of RRDE electrode.

Gravimetric Gas Sorption Measurement Over a Wide Pressure Range

The vapor adsorption capacity of CO_2 and m-xylene on the prepared carbon nanostructures was evaluated with the IsoSORP STATIC 3Xv-MP gravimetric gas sorption system, which involves a Magnetic Suspension Balance (Rubotherm, Germany) and has the capacity to perform gas or vapor sorption measurements over a wide range of temperatures and pressures.

Each sample was initially degassed under high vacuum at 150 °C until mass stabilization. Given the mass and the volume of the balance's magnetic coupling components (sample crucible, suspension shafts) and the mass of the degassed sample, the balance reading (apparent mass) was corrected for the buoyancy effect (mass of displaced gas) with the prerequisites that the change of density of the gas phase was recorded in situ and the volume of the sample was calculated (both parameters automatically measured by the instrument). The corrected mass values of adsorbed gas or vapor per unit of sample mass (mg g^{-1} or mmol g^{-1}), were automatically recorded at each equilibrium point after the sample exposure to a specific gas or vapor pressure at a constant temperature.

Results and Discussion

Study of the Carbonization/Activation Process

The mass loss of each unconfined samples prepared through the carbonization/activation process was systematically recorded as a function of time during each phase of the process (N_2-flushing/temperature ramping/isothermal stage/CO_2-activation). Monitoring the mass loss evolution offered hints to draw conclusions on the extent of the formed pores, especially during the activation stage, thus defining the most effective porogenic approach.

In the first method the nanostructured porous carbon was produced through two successive pyrolytic/activation treatments with a total CO_2 activation time of 4 h. Hereinafter, this sample is denoted as C-4 h and its mass loss evolution is shown on Figure 2a; red and blue curves account for the first and second pyrolytic/activation treatment, respectively.

The other carbon formation method encompassed one pyrolytic/activation treatment only with a total CO_2 activation time of 8 h. We refer to this sample as C-8 h and its mass loss evolution is outlined on Figure 2b.

As depicted in Figures 2a,b, all thermal treatments started by flushing samples with N_2 gas. Then, the temperature was increased gradually at a rate of 10 °C/min up to 800 °C. During this heating phase the mass of C-4 h attenuates sharply up to 400 °C (Figures 2a,b) as the consequence of a fast IL thermal degradation.[16,37] Afterwards, the sample C-4 h was kept at 800 °C (isothermal conditions) for 20 min. Within this period the mass loss rate was almost constant and stable (Figure 2a, Table 1).

After the isothermal step, the sample C-4 h was activated for ~1 h under CO_2 flow (100 mL/min), whereas sample C-8 h was activated for ~8 h without having been previously subjected to an isothermal step. During activation the rate of sample mass loss was slightly amplified (Figures 2a,b and Table 1).

Compared to other studies of carbon activation with CO_2,[38] the total mass loss % measured for C-4 h during the first pyrolytic/activation treatment was appreciably lower likely due to a reduced extent of pores formed during this step. An additional pyrolytic/activation treatment was accomplished on the sample with a longer activation time, necessary to improve the sample porosity. Despite the moderate mass loss, the fact that the second cycle of pyrolysis/activation started with a net mass higher than that possesses upon completion of the first cycle (Figure 2a), was indicative of pores formation. Indeed, during the sample cooling under N_2 atmosphere, its porous structure adsorbed nitrogen, CO_2 and any moisture traces of gaseous molecules produced during the thermal phase and trapped into the tubular furnace. Accordingly, it can be stated that part of the intense mass drop observed during the second

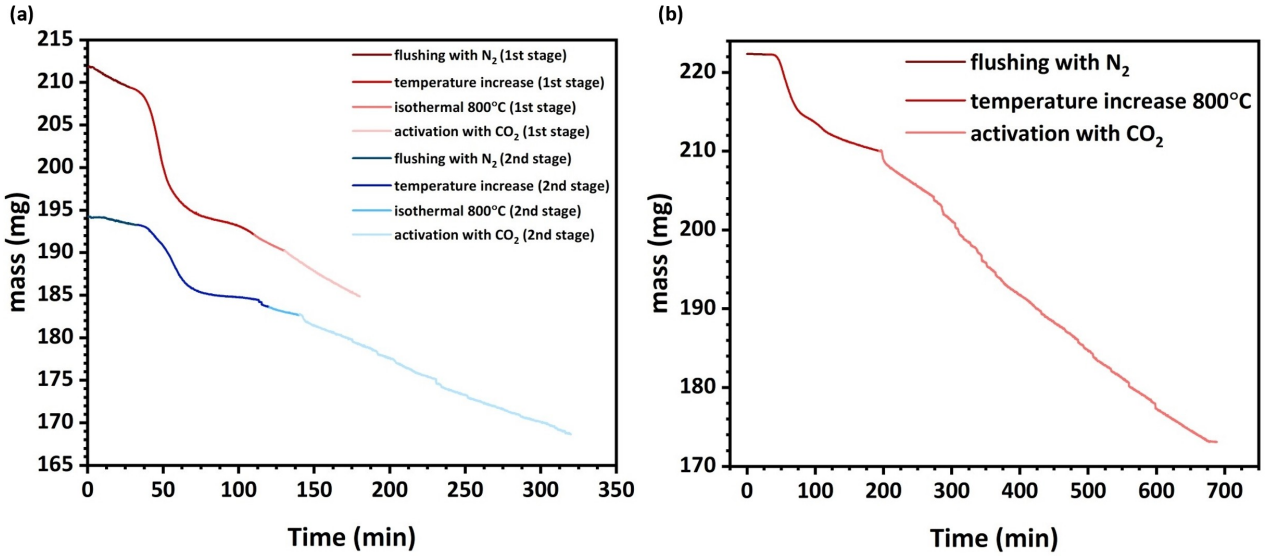

Figure 2. (a) Mass loss evolution during the heat treatment of an unconfined IL after two thermal cycles of pyrolysis/activation (sample C-4 h); (b) Mass loss evolution during the heat treatment of an unconfined IL after one single thermal cycle of pyrolysis/activation (sample C-8 h).

Table 1. The rate of mass loss during the pyrolysis/activation steps of [BMIM][TCM] (slope values) and the respective % mass losses.

	Isothermal stage		Activation stage	
Sample	slope (mg min^{-1})	mass loss (%)	slope (mg min^{-1})	mass loss (%)
C-4 h (first cycle)	−0.092	0.94	−0.107	2.82
C-4 h (second cycle)	−0.044	0.51	−0.078	8.40
C-8 h	–	–	−0.077	17.62

calcination stage was due to the occurrence of gaseous desorption phenomena. This is further confirmed by the fact that we registered the same sample mass both at the beginning of the isothermal stage (second thermal run) and at the end of the first pyrolytic/activation treatment (Figure 2a).

The isothermal stage of the second thermal run lasted for 20 min, while the activation stage was prolonged up to 3 h. The slightly slow rate of mass loss during the second activation stage was ascribed to surface oxidation phenomena, likely accompanied by the generation of O-containing functional groups. As heat treatment continues, the functional groups can remain on the material surface, creating strong adsorption sites for various gaseous molecules, or decompose with the evolution of volatiles leaving behind highly defective C-sites that can be involved in turn as preferentially adsorption sites of the carbonaceous nanoarchitecture.

Comparing mass loss rates measured for the two samples C-4 h and C-8 h during the activation stage (Table 1), it is possible to conclude that their profiles are almost superimposable and thus identical, whereas the respective total mass losses % correlate almost linearly with the activation times. However, this does not apply in the case of long-time activation treatments (Figure 3) where the mass loss % starts to diverge significantly from linearity. In addition, N_2 physisorption analysis carried out for the measurement of the sample's porosity (in following section: N_2 adsorption (77 K) measurements) has unveiled that the pores volume is not linearly correlated with the CO_2 activation time. On the other hand, mass loss % and pore volume follow a strictly linear correlation ($R^2 = 1$). This implies that following the mass loss % during the activation phase allows the fine control of porosity in the activated carbon sample.

N_2 Adsorption (77 K) Measurements

The porous structure of developed carbons was elaborated by interpreting the results of N_2 adsorption at 77 K. Samples isotherms were obtained on a Quantachrome porosimeter after degassing each sample at 250 °C overnight. BET (Brunauer-Emmett-Teller) method was applied to the calculation of the specific surface areas (SSA) of each sample, while pore size distributions (PSDs) were obtained using the Quenched Solid Density Functional Theory (QSDFT) method. The PSDs were derived from both the adsorption and desorption (equilibrium) branches of the isotherm. QSDFT was selected as the most realistic theoretical analysis model for carbonaceous materials prepared via the templated precursor path and thus applied to samples featured by wrinkled and rough amorphous pore walls, the alternative NLDFT model was more appropriate in the case of porous carbons with flat and non-structured graphitic walls.[39]

In a previous work,[25] we presented that the morphology of the hard template (mold) was pivotal for the development of robust and uninterrupted carbon replicas. The existence of pore necks is an asset of Vycor® hard templates that hampers to get continuous carbon frames. This is due to the shrinkage of the IL during the pyrolytic treatment that causes the formation of nanosized carbon domains inside of the Vycor® pores. Pore necks cause the loss of connectivity of the C-network or generate so thin links that are invariably broken by the chemico-physical stress the sample undergoes during the dissolution of the hard template. To overcome these physical and mechanical limits, we applied the pore etching process described in section 3.2 with the final aim of widening the pore necks and thickening carbon domains lying into their cavity. Accordingly, the duration of the pore etching procedure is a critical issue that led us to conclude that five hours of hydrofluoric acid (HF) etching on Vycor® samples were not enough to sufficiently widen pore necks as to provide inverse replica structures featured by continuous carbon nets.[25] Hereupon, a justification of this statement is provided. As such, the width of the solid domains of Vycor® should be ca. 160 Å (~7/3×68 Å), where 68 Å is the mean size of Vycor® pores as derived by applying the NLDFT method on the adsorption branch of the isotherm. Considering also the N_2 adsorption (77 K) results of the eps-Vycor® samples (Table 2), the respective solid domains of 2HF-Vycor®, 3HF-Vycor®, 5HF-Vycor® should be 143, 143 and 130 Å. The width of the glass solid domains should be equal to the pore size of the C-samples, provided that these are extracted as a continuous inverse replica of the Vycor® templates.

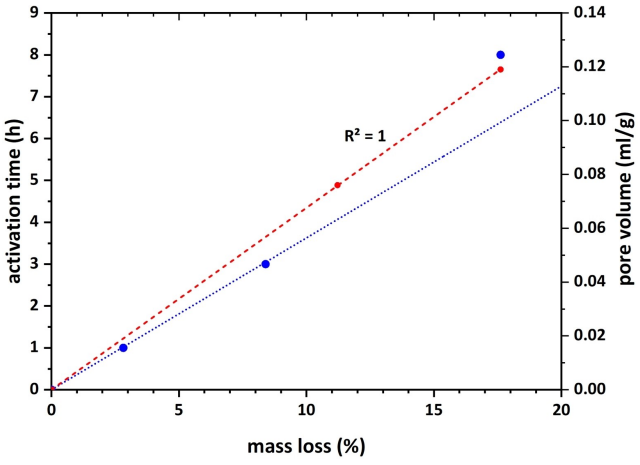

Figure 3. Dependence of the % mass loss on the activation time and pore volume. (large blue cycles-activation time), (small red cycles-pore volume).

Table 2. Effect of the etching period on the size of the bulk pores and necks of Vycor®. The expected size of the solid domains of Vycor® is also included.

Eps-Vycor® samples	Average pore size NLDFT ads. (Å)	Average Neck size NLDFT des. (Å)	Solid domain size (Å)
Vycor®	68	63	160
2HF-Vycor®	85	63	143
3HF-Vycor®	85	76	143
5HF-Vycor®	98	91	130

The most significant size amplification of the bulk pores and necks in Vycor® took place after 5 h of chemical etching (Table 2) although the carbon network produced from this template (5HF- Vycor®) still does not maintain the continuity of its replica structure. This conclusion is confirmed by the average mesopore size (~100 Å) of the carbon sample (Figure 4b) in spite of 130 Å as expected average pores size. The same conclusion applies to the carbon obtained after 7 h etching (Figure 4b-average mesopore size ~100 Å). Though the inverse replica structure collapsed, both these carbons exhibited enhanced pore structural properties for application in electrochemical and adsorption processes.

More in details, both carbons presented a multi-modal PSD, encompassing micropores with a size centered around 12–13 Å, along with two types of mesopores with sizes centered at 39–42 Å and 99–107 Å (Figure 4b). The micropores are of slit-like shape and constitute an inherent pore structural characteristic of the formed carbon nanodomains, whereas the mesopores of different size are formed due to the collapse of the inverse replica structure. Mesopores of smaller size (i.e., 39—42 Å) are associated with voids that exist within the rigid nanosized sections of the initially developed inverse replica skeleton. These sections are formed upon the collapse of the carbonaceous skeleton and consist of strongly agglomerated carbon nanodomains. On the other hand, the larger mesopores represent voids existing within two additional carbonaceous structural entities that are also formed due to the collapse of the inverse replica's skeleton. The first one consists of loose assemblies of the above-mentioned carbon sections (small fragments of the inverse replica frame), having pores with sizes gathered on the left side of the arithmetic mean of the bell-shaped PSD curve (Figure 3b). These sizes extent from 50 Å to 100 Å. The second structural entity consists of larger fragments that possibly retain, up to a short length scale, the inverse silica structure. The size of the pores (100 Å to 165 Å) correlates well with the expected size of the solid domains in the involved eps-Vycor® hard templates (130 Å, Table 2).

It can be argued that the carbons derived from the long period etched eps-Vycor® (e.g., 5 and 7 h) share common pore structural characteristics. However, there are distinct features between these two carbon samples, relatively to the shape of the N_2 adsorption isotherms and the way the PSD curves decay at the region of large pore sizes (Figures 4a, b). The different shape of the N_2 adsorption isotherms and PSD curves is attributed to the different portion of the small and large fragments in these two samples.

In specific, there is a noticeable shoulder-like section on the PSD curve of the carbon sample derived from the 7HF-Vycor® template (Figure 4b). The shoulder appears at a mean pore size, which is equal to the size of the solid domains of the hard template (130 Å). Conclusively, the carbon derived from the 7 h etched template possesses a greater portion of large carbonaceous fragments that are of sufficient scale and rigidity to retain the inverse replica structure. It can be also claimed that the pore structural characteristics of this sample approximate those expected by the continuous inverse replica of the template. Thence, prolonging the etching time from 7 to 8 h could be enough to yield a material with the targeted pore structural characteristics. On the other hand, the carbon derived from the 5 h etching of the solid template presented a type IV N_2 (77 K) adsorption isotherm with open hysteresis branch (Figure 4a). This feature is usually attributed to pressure-dependent elastic deformation of flexible porous networks that in our case is related with the existence of large-scale carbonaceous fragments of moderate rigidity. Therefore, the carbon derived from the 5 h etched template is still characterized by the existence of ultra-thin carbon sections (those formed at the pore necks of the template) that sprawl on the entire carbon skeleton, significantly suppressing its rigidity.

As regards the activated carbon samples, C-4 h and C-8 h, produced with the technically easy pathway of pyrolysis/

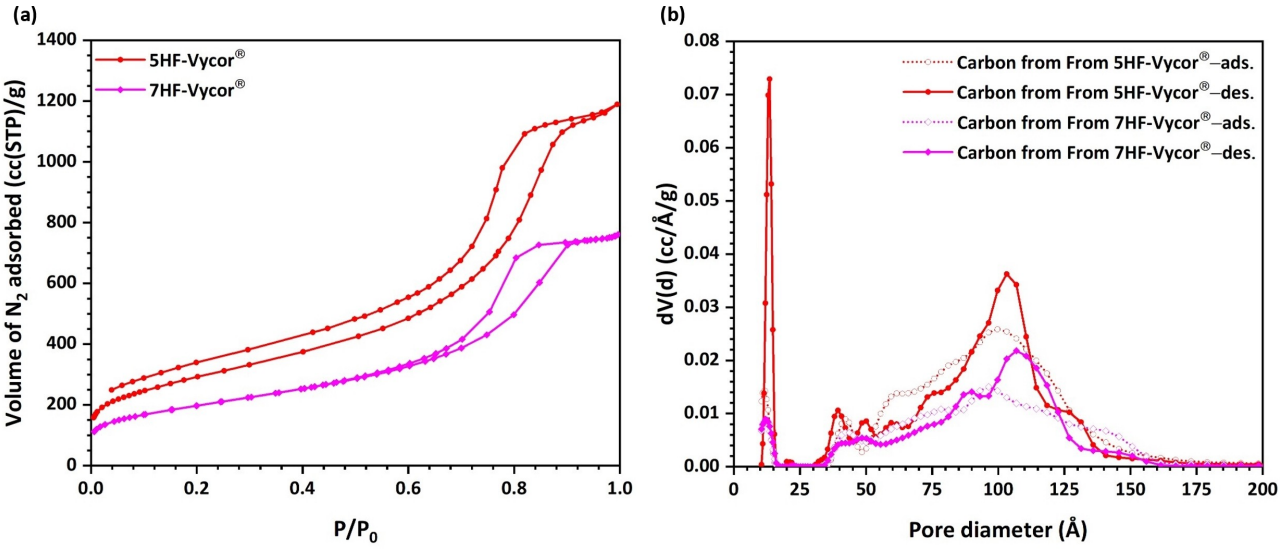

Figure 4. (a) Comparison between the N_2 adsorption isotherms at 77 K of the carbon samples derived from 5HF-Vycor® and 7HF-Vycor®; (b) Comparison between the PSDs of the carbon samples derived from 5HF-Vycor® and 7HF-Vycor®.

activation of the unconfined [BMIM][TCM], their N_2 adsorption isotherms at 77 K are presented in Figure 5, and they are compared to that of a carbon sample (char), which was derived by simply implementing the pyrolytic treatment of the bulk IL precursor. It should be noticed that all the steps of pyrolytic treatment (N_2-flushing/temperature ramping/isothermal stage) for the fabrication of these three samples were performed under identical conditions.

Table 3 summarizes the main properties of C-4 h and C-8 h samples related to their pore structural characteristics. An initial noteworthy remark (Figure 5) is that the N_2 adsorption isotherm (77 K) of the pyrolyzed bulk IL (free [BMIM][TCM]) signifies the complete absence of pores, denoting that the yielded carbon sample was a non-porous solid char. It can be concluded that the IL's nanoconfinement is responsible not only for the formation of an extended mesopore structure but also for the creation of micropores as an inherent characteristic of the generated carbonaceous nanodomains. It can be also deduced (Figure 5, Table 3) that the activation process with CO_2 etches micropores into the char material and that the formed micropore volume is much less compared to the micropore volume of the carbons produced via the templated precursor pathway. In spite of that, both activated carbons from pyrolysis/activation of unconfined bulk IL (C-4 h and C-8 h) are promising materials for several applications due to the uniformity of their pore structure and their chemical composition not deeply affected by the process, especially in terms of N-dopants.

Another interesting feature is that the pore size remains almost unchanged independently from the mass loss and the period of activation (Table 3, Table 1). This can be explained by the existence of nanosized areas within the pyrolyzed carbon structures, which are more vulnerable under the non-so aggressive conditions of physical activation with CO_2.

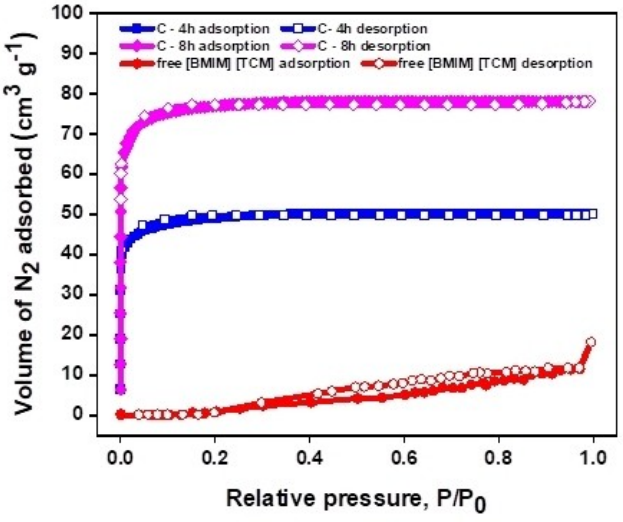

Figure 5. N_2 adsorption isotherms at 77 K of C-4 h and C-8 h, compared to the adsorption isotherm of a carbon sample derived by pyrolyzing [BMIM][TCM] at 800 °C in its free state.

Catalytic Performance of Recovered Carbon Nanostructures in Oxygen Reduction Reaction

Despite that the carbons derived from the etched pore glasses 2HF-Vycor®, 3HF-Vycor® and 5HF-Vycor® were relatively far from having the structure of the inverse replica of the hard template, they were selected as carbon-based catalytic materials for the challenging electrochemical ORR due to their multimodal pore size distribution along with very high pore volume and specific surface area, which surpassed those of the carbon from 7HF-Vycor® (Table 4). Cyclic voltammetry (CV) measurements (not reported here for the sake of shortness) were initially carried out with samples 2, 3 and 5HF-Vycor® both under N_2 and O_2 atmosphere with the target to assess the electrochemical ability of these N-doped C-materials to activate and reduce electrochemically dioxygen.

Table 3. Characteristics of the porous structure of C-4h and C-8h samples.

Sample	S_{BET} ($m^2 g^{-1}$)	Total Pore Volume (TPV) ($cc\,g^{-1}$)	Mean pore diameter (d) (nm)
C-4 h	148.8	0.076	2.04
C-8 h	229.2	0.119	2.08

Table 4. Pore structural characteristics of carbons derived with the templated precursor pathway from short- and long-period etched Vycor® templates. Results were produced from the N_2 adsorption/desorption isotherms (Figure 4a).

Carbon samples	Surface area (BET) (m^2/g)	Micropore volume (mL/g)	Mesopore volume (mL/g)	Macropore volume (mL/g)
From 2HF-Vycor®	1012	0.37	1.01	–
From 3HF-Vycor®	930	0.34	0.80	–
From 5HF-Vycor®	1042	0.38	1.46	–
From 7HF-Vycor®	703	0.26	0.92	–
Commercial Carbon AC 40. Ref. [40–43]	1200	0.40	0.05	0.41

Afterwards, all elaborated electrocatalysts were scrutinized with the Rotating Ring Disk Electrode (RRDE) and the corresponding voltametric curves are depicted in Figure 6.

As it can be seen from the analysis of these electrochemical profiles, all electrocatalysts shown a well-defined ORR reduction peak with remarkable onset potential values (Eon) (Table 5).

In particular, all samples displayed only 20–30 mV of overpotential compared to the Pt reference electrode (Figure 6 and Table 5). Noteworthy, all samples also exhibited moderate ring currents (Figure 7a) that are indicative of very low amount of H_2O_2 % produced (Figure 7b). These data are consistent with a very efficient oxygen reduction with an average number of exchanged electrons (n) at −1 V as high as 3.8 and 3.9 for samples 2, 3 and 5HF-Vycor®, respectively (Table 5).

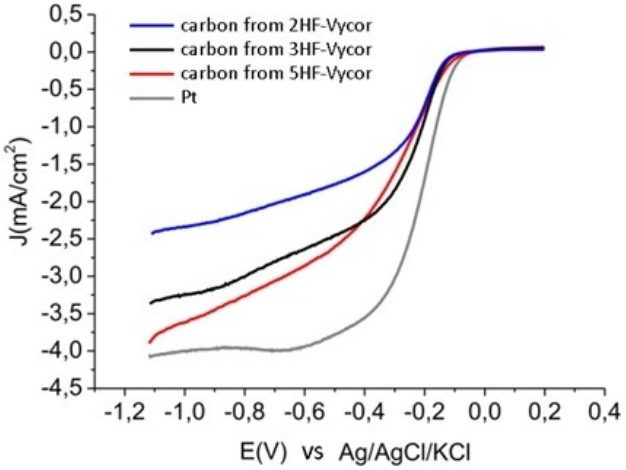

Figure 6. RRDE current-potential curves of carbon from 2, 3 and 5HF-Vycor® at 293 K in O_2 saturated 0.1 M KOH solution registered at GC disk (A = 0.196 cm^2). All samples were measured at a working electrode spin rate of 800 rpm.

Table 5. Eon (V) values, H_2O_2 (%) and n at E = −1 V as calculated from H_2O_2 (%) of carbon samples from 2, 3 and 5HF-Vycor® as compared with Pt.

Samples	Eon (V)	H_2O_2 (%) (E = −1 V)	n (E = −1 V)
Carbon from 2HF-Vycor®	−0.13	9	3.8
Carbon from 3HF-Vycor®	−0.13	8	3.8
Carbon from 5HF-Vycor®	−0.12	6	3.9
Pt	−0.10	–	–

Adsorption Performance of Carbon Nanostructures for M-Xylene Vapor

In the context of this study, samples with quite distinct pore structural features were examined for their m-xylene vapor adsorption capacity. A first important difference is that the micropores in the samples derived with the templated precursor pathway (carbons from 2HF-Vycor®, 5HF-Vycor® and 7-HF Vycor®) exhibited values comprised between 10–12 Å, whereas those of the carbon C-8 h had mean size of 20 Å. Furthermore, the carbons derived via the templated precursor pathway exhibited much higher micropore volume values as compared to carbon C-8 h, along with an extended multi-modal mesopore structure that was completely absent from sample C-8 h. Notably, there were also significant differences between the pore structures of samples developed with the templated precursor pathway (Figure 8).

As such, carbons derived from a short period etched template (2HF-Vycor®) had highly hierarchical porous structures with a PSD curve showing distinct peaks at 120, 75, 45, 40, 25, 15 and 11 Å. Apart from that, other differences in terms of chemical composition of the samples may exist. They relate with the content of the structural nitrogen from pyridinic, pyrrolic and quaternary graphitic groups[43] within the carbon nanodomains, as well as with the surface population and type of functional groups (oxygenated functional groups or abundant surface nitrogen). It has already been presented that the introduction of structural nitrogen enhances the surface polarity of the C-adsorbents, inducing a strong electric dipole moment for CO_2, thus forming acid-base pairs, hydrogen bonds and

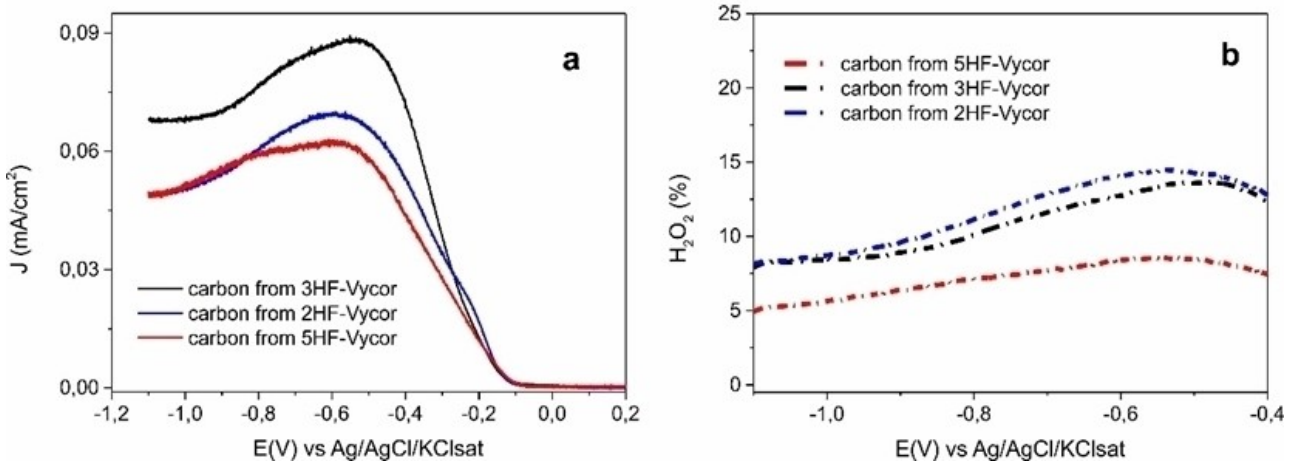

Figure 7. (a) Density current (J) registered at Pt ring (A = 0.11 cm^2) for carbon samples from 2, 3 and 5 HF-Vycor® and (b) the corresponding H_2O_2 (%) produced.

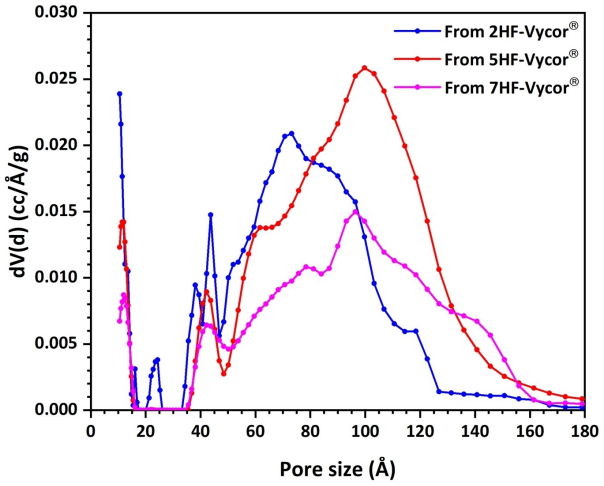

Figure 8. PSDs of the carbons examined as m-xylene ad-sorbents (derived from QSDFT-adsorption branch of N_2 isotherm at 77 K).

other interactions that augment the adsorption capacity and selectivity of CO_2.[44] Moreover, the coexistence of adjacent pyridinic and –OH/–NH_2 has a significant contribution to the enhancement of CO_2 adsorption capacity,[45] while amongst the three types of structural nitrogen the pyridinic N-5 structures are better for CO_2 adsorption.[46] Amongst the oxygenated groups the structure of –OH contributes more to CO_2 adsorption than those of –COC– and –COOH.[46] In a previous work, we have concluded that the carbons produced through the pyrolytic treatment of the ionic liquid [BMIM][TCM] (at 800 °C) confined into a Vycor® template, exhibited a nitrogen content of about 18 wt%.[25] Moreover, the N-content depended on the maximum carbonization temperature and not on the pore size of the etched Vycor® template. On the contrary, the carbons developed by the free-unconfined precursor pathway and further activated with CO_2, exhibited much lower nitrogen content and high oxygen content. Hence, despite the early (at 300–400 °C) participation of nitrogen in the formation of the stabilizing oligomers, the further densification and evaporation of nitrogenous by-products above 500 °C was proved to be more controllable with the templated precursor pathway due to the effect of nanoconfinement that limits the evaporative losses. In contrast with the use of the molten alkali hydroxides activation technique, the less drastic but technically easier approach of activation with CO_2 did not significantly change the N-dopants content of the samples. However, it brings to high oxygen content due to surface oxidation. Accordingly, it is expected that differences in the m-xylene vapor adsorption capacity of the samples will be primarily governed by differences in the pore structure and secondarily by variations of the samples surface chemistry.

The adsorption isotherms of m-xylene were obtained with the gravimetric technique described in aforementioned Section (Gravimetric gas sorption measurement over a wide pressure range). The experiments were conducted at two different temperatures (25 and 45 °C) and the maximum relative pressure (P/P_0) reached in each temperature was 0.63 and 0.69, respectively. At 25 °C we proceeded with pressure steps of 1 mbar, while larger pressure steps were applied in the experiments performed at higher temperature. Figure 9 illustrates the relevant m-xylene adsorption isotherms of all samples, while Table 6 demonstrates the adsorption capacity of the samples at specific relative pressures for m-xylene vapors as adsorbate.

As a head start for our survey, we created correlation plots (depicted in Figure 10) that are representative for the relation between the pore structure (micropore, mesopore and total pore volume) of the examined samples and the adsorbed amount of m-xylene (adsorptivity) at selected conditions of temperature and pressure.

Comparing Figures 10a,b, that enclose the adsorption capacity obtained at low relative pressure ($P/P_0 = 0.27$) and two

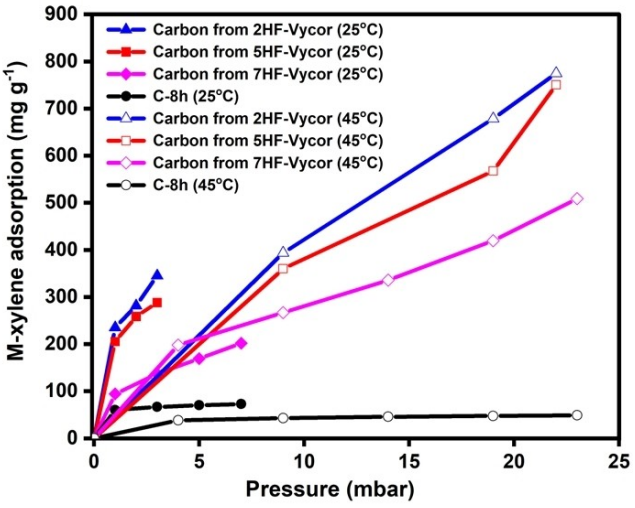

Figure 9. M-xylene sorption isotherms for carbons from 2, 5 and 7HF-Vycor® and for C-8 h, at temperatures 25 and 45 °C.

Table 6. Maximum adsorbed mass of m-xylene at temperatures 25 and 45 °C and at pressure 3 and 19 mbar for carbons from 2, 5 and 7HF-Vycor® and for C-8 h.

Sample	Amount of m-xylene at 25 °C and 3 mbar ($P/P_0 = 0.27$) (mg g^{-1})	Amount of m-xylene at 45 °C and 19 mbar ($P/P_0 = 0.57$) (mg g^{-1})	Amount of m-xylene at 45 °C and 9 mbar ($P/P_0 = 0.27$) (mg g^{-1})
2HF-Vycor®	345.4	678.6	394.9
5HF-Vycor®	288.1	567.5	358.9
7HF-Vycor®	136.9	419.2	265.1
C-8 h	66.7	47.6	43.2

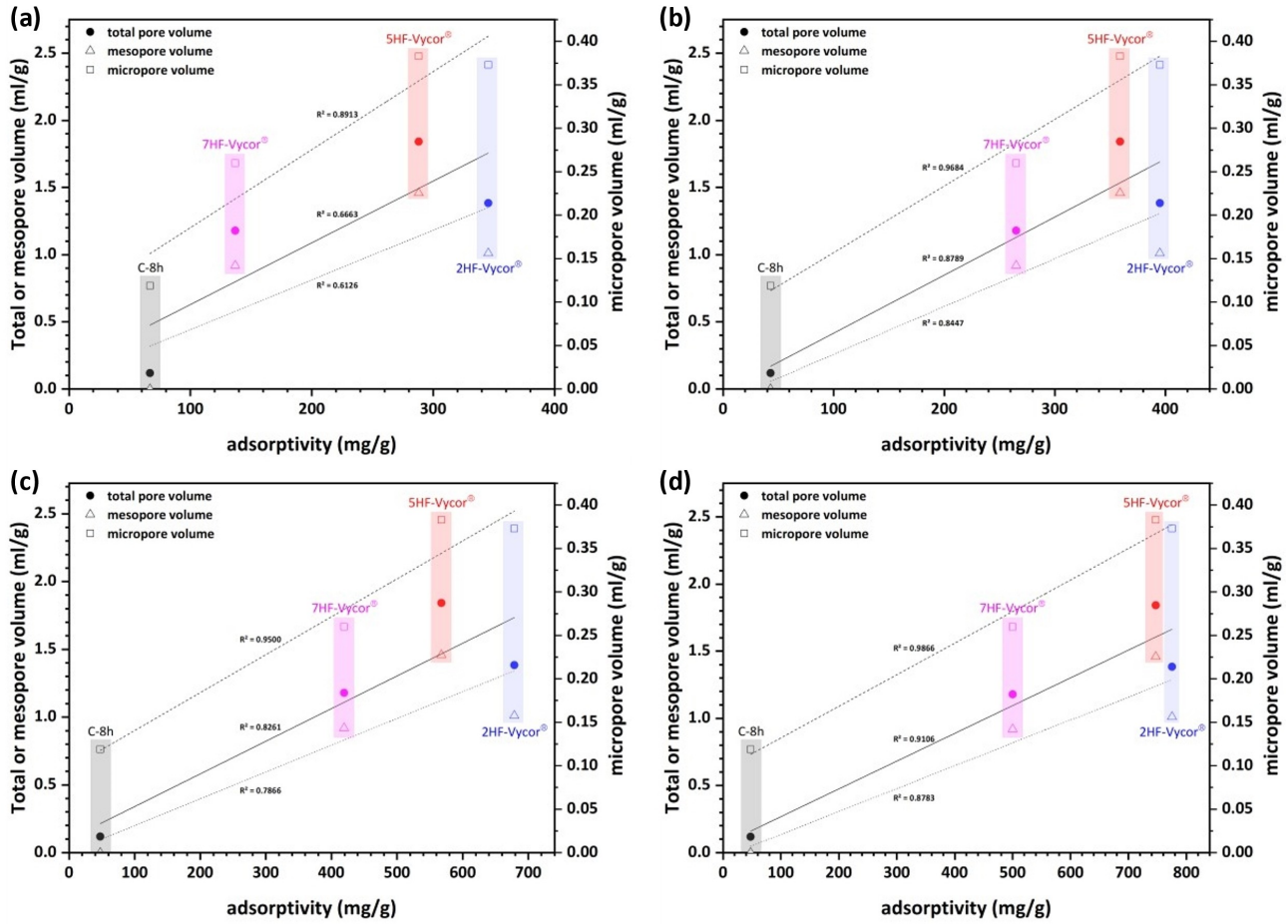

Figure 10. Correlation between the m-xylene adsorption capacity and the pore structural characteristics at different conditions: (a) 25 °C, $P/P_0 = 0.27$; (b) 45 °C, $P/P_0 = 0.27$; (c) 45 °C, $P/P_0 = 0.57$; (d) 45 °C, $P/P_0 = 0.69$.

different temperatures (25 °C and 45 °C, respectively), it can be concluded that the best linear fitting, having a correlation coefficient close to unity (R^2 ~1), holds between the values of the micropore volume and the m-xylene adsorptivity at 45 °C. The dependence of the micropore volume on the adsorptivity deviates a bit from linearity at 25 °C (R^2 ~0.9), whereas in all cases the mesopore and total pore volume are far from having a linear correlation with the adsorbed amount of m-xylene. This means that the prevailing structural features that define to a high extent the adsorption capacity of the samples are the size and volume of the micropores. Focusing on the correlation of micropore volume vs. m-xylene adsorptivity (Figure 10a), it becomes clear that the deviation is positive for samples C-8 h and 2HF-Vycor® and negative for the other two samples produced via the templated precursor pathway. A positive deviation from the trendline reflects a sample that exhibits higher adsorption capacity (and vice versa) despite having a lower micropore volume. It is noteworthy that the two samples presenting positive deviation are those holding larger micropores into their structure. Carbon C-8 h, having a uniform PSD of micropores centered around 20 Å, and the carbon from 2HF-Vycor®, exhibiting a multimodal PSD with micropores of 25, 15 and 11 Å, do not exert much hindrance to the passage and diffusion of the m-xylene molecules into the micropore cavities. On the contrary, carbons from 5HF- and 7HF-Vycor®, possessing a uniform PSD of narrow micropores (centered at 10 Å), inhibit appreciably the entrance of bulky m-xylene molecules.

Consequently, m-xylene molecules must overcome a larger energetic barrier to pass directly from the gas phase inside the pore and be adsorbed near the pore mouth. The probability for direct entrance enhances at higher temperatures and this explains the much better linear fittings obtained between the values of micropore volume and m-xylene adsorptivity at 45 °C (Figures 10 b–d). However, the fact that the higher temperature gives rise to enhanced adsorptivity of m-xylene is contradicting to what expected by the exothermic adsorption process. Apart from the better correlations obtained at 45 °C (Figure 10), the beneficial effect of temperature is also apparent from the data presented in Table 6. Hence, for the same relative pressure ($P/P_0 = 0.27$), the amount of adsorbed m-xylene is higher at 45 °C than at 25 °C, and this holds for all the carbon samples except for C-8 h.

Furthermore, higher amplifications in adsorptivity values are observed for the carbons with narrower micropores (from 5HF- and 7HF-Vycor®). A justification on these issues is that the points of the isotherms obtained for the carbons from 5HF- and

7HF-Vycor® (Figure 9), do not represent the real adsorption equilibrium points. This is related to the multimodal pore structure of these samples in conjunction with their very narrow micropores and the algorithm embedded in the software of the gravimetric sorption analyzer to fit the transient curve (mass uptake vs. time) and deduce whether sorption equilibrium has been reached. As such, immediately after the application of each pressure step, the mass of the sample increases suddenly because m-xylene molecules diffuse without any hindrance into the mesopores and are adsorbed on their pore walls. As soon as adsorption into the mesopores reaches equilibrium, the transient curve appears misleadingly to have reached a plateau, while adsorption into the micropores continues, evolving so slow that it does not bring any appreciable variation in the mass uptake rate. Hence, the algorithm considers this as an equilibrium and triggers the initiation of the next pressure step, leading to underestimated values of adsorptivity. We have also exploited the capability of the software of the sorption gravimetric analyzer to implement the sequence of pressure dosing on a time-limit basis. Though we have selected a period of 3 hours as enough for the sample to reach adsorption equilibrium at each pressure step, the adsorptivity of m-xylene at 25 °C was again underestimated. Apparently, there is a threshold in the size of the micropores, below which, the adverse effects of restricted diffusion on the adsorptivity of the bulky m-xylene molecules (kinetic diameter of 6.8 Å[48]) are activated. It seems that micropores of size less than 15 Å start to become hardly accessible to the m-xylene molecules.

To adduce further evidence on this issue, Figure 11 presents the m-xylene vapor adsorptivities of the carbons developed in this work via the templated precursor pathway, in comparison to the performances of other types of activated carbons found in the literature. The comparison is made at two different temperatures (25 °C and 45 °C). Compared to the commercial AC 40 (CECA S.A.) material,[40] a chemically activated carbon with a specific surface area of 1200 m^2/g used in many applications as a benchmark adsorbent,[41–43] our samples showed lower m-xylene adsorptivity at 25 °C (Figure 11a) and equal or even higher adsorptivity at 45 °C (Figure 11b).

While the carbons from 2HF- and 5HF-Vycor® exhibited significantly high surface area (~1100 m^2/g) that was comparable to that of AC 40, their distinct pore structural characteristics were the presence of extended mesoporosity, instead of macroporosity (pore width >50 nm) (Table 4), and the existence of quite narrow micropores (<15 Å) that possessed a large fraction of the total micropore volume, whereas the mean micropore size of AC 40 was 20 Å.[40] At 25 °C, micropores of samples 2HF- and 5HF-Vycor®, featured by mesopore volumes of 1.01 and 1.46 mL/g, respectively, did not contribute significantly to the m-xylene adsorption capacity. However, despite that commercial carbon AC 40 exhibits a total pore volume of 0.86 mL/g (micro + meso + macro), which is much lower than the mesopore volume of the carbons 2HF- and 5HF-Vycor®, it presented significantly higher m-xylene adsorptivity.[40] This constitutes further evidence that the prevailing mechanism for the high uptake capacity of m-xylene is the adsorption into micropores. In specific, the existence of wide micropores is the optimum structural feature, while smaller micropores start to contribute at higher temperatures, where restriction effects are weakened due to the enhanced kinetic energy of gas molecules. Comparing the adsorption capacity of the three samples developed with the templated precursor pathway (2HF-, 5HF- and 7HF-Vycor®) unveils that the next most contributing feature is the size and hierarchical structure of the mesopores.

Focusing on the m-xylene adsorption results at 25 °C and $P/P_0 = 0.27$ (Table 6), the sample 2HF-Vycor® presented the highest adsorptivity, as expected due to its significant fraction of micropores with size centered around 20 Å. Furthermore, focusing on the results at 45 °C and $P/P_0 = 0.27$, it could be expected that the m-xylene adsorptivity would correlate linearly with the total (micro and meso) pore volume (TPV) of the

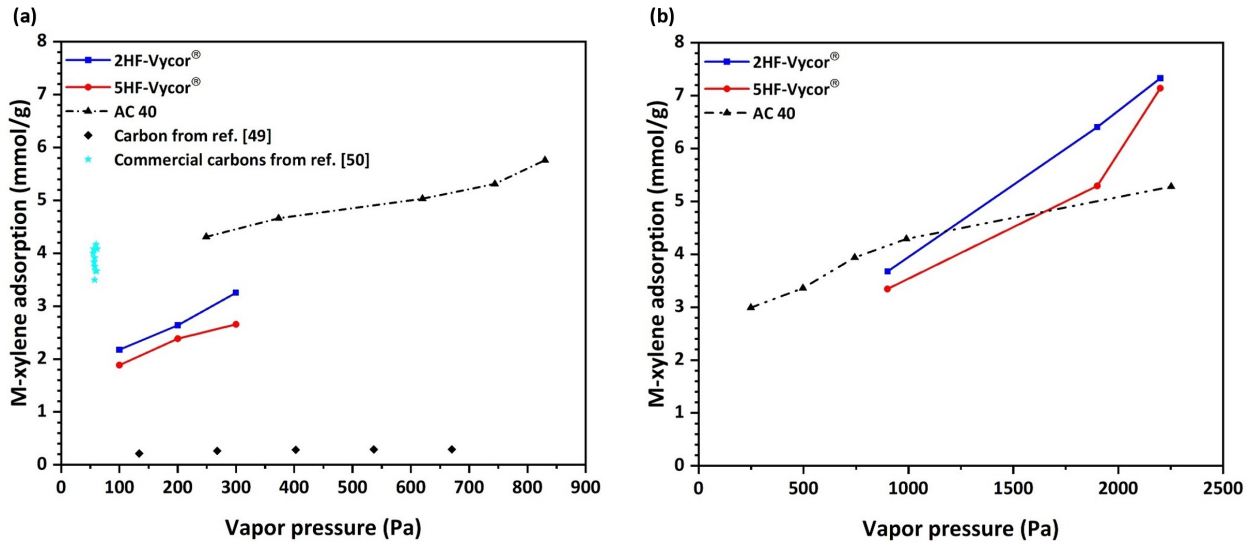

Figure 11. Comparison of the m-xylene adsorption capacity between the best performing carbons of this work and commercial carbons used as benchmark materials at: (a) 25 °C; and (b) 45 °C.

samples. However, sample 2HF-Vycor® was again the best performing one, despite its significantly lower total pore volume as compared to 5HF-Vycor®. Moreover, the TPV ratio between samples 2HF-Vycor® and 7HF-Vycor® was 1.17, while the respective ratio of m-xylene adsorptivities was 1.5.

As a general outcome it can be stated that the m-xylene adsorptivity of activated carbons is highly affected by the population of active adsorption centers and the pore structural features of the samples. In this work, however, we had the opportunity to compare samples having identical populations of active sites and quite different pore structure. This feature has already been validated in a previous work, which showed that for ACs derived from IL precursors with the templated precursor pathway, the pyrolysis temperature and the period of pyrolysis are the crucial factors affecting the content of heteroatoms in the produced carbons. Hence, since all the Vycor® templated samples were prepared with 2 h of pyrolysis at 800 °C, it was reasonable to consider identical percentages of N-doping. Overall, analyses disclosed that micropores with a size centered around 20 Å and small mesopores were the most beneficial for the enhancement of m-xylene vapors adsorptivity.

Adsorption Performance of Carbon Nanostructures for CO_2

One distinguishing feature between CO_2 and m-xylene is represented by the smaller kinetic diameter of CO_2 and its higher quadrupole moment. Hence, contrarily to what holds for m-xylene, the best adsorbents for CO_2 must be those exhibiting purely micropore structure consisting of narrow micropores.[1] To validate the above statement, we investigated the CO_2 adsorption performance of samples C-4 h and C-8 h, which displayed purely microporous structures with a bimodal pore size distribution characterized by quite narrow micropores and wide mesopores. Additionally, sample C-4 h, possesses the less N-content among the three samples and significantly higher O-content due to the 4 h activation with CO_2. Sample C-8 h exhibits the highest amount of oxygenated functional groups and moderate N-content, while the carbon sample from 7HF-Vycor® holds the highest N-content and no oxygenated functionalities.

The CO_2 adsorption isotherms were carried out at 25 °C and were determined by the gravimetric method at pressures up to 1 bar. The corresponding isotherms are shown in Figure 12, while Table 7 includes the maximum CO_2 adsorption values for each sample at ambient pressure (1 bar).

It is remarkable that contrarily to what happened with the adsorption of m-xylene (see Figure 9 and Table 6), samples C-8 h and C-4 h present higher CO_2 adsorptivity compared to the carbon nanostructure from 7HF-Vycor®. As can be seen (Figure 12), the adsorbed amount of CO_2 for the whole range of applied pressures was greater for sample C-8 h. Also, whereas up to 550 mbar the adsorbed amount of CO_2 from sample C-4 h exceeded the corresponding amount adsorbed from the 7HF-Vycor® carbon, this trend is inversed at higher pressures up to 1 bar. In the following paragraphs, an explanation is provided on account of the above findings in relation to the pore

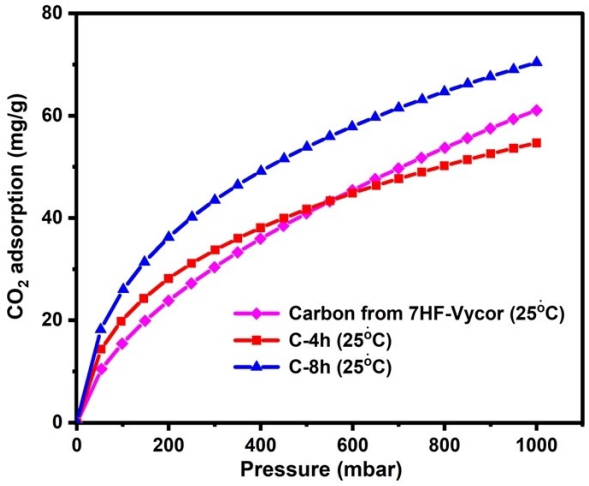

Figure 12. CO_2 adsorption isotherms for carbon from 7HF-Vycor® and for C-4 h and C-8 h, at temperature 25 °C.

Table 7. Maximum adsorbed mass of CO_2 at temperature 25 °C and at pressure 1 bar for carbon from 7HF-Vycor® and for C-4 h and C-8 h.

Sample	Maximum adsorbed mass of CO_2 ($mg\,g^{-1}$)
7HF-Vycor®	61
C-4 h	55
C-8 h	70

structural characteristics and the variations in the surface chemistry of the three examined samples. Hence, the presence of the oxygen groups in samples C-4 h and C-8 h seems to suppress the m-xylene's adsorptivity. On this basis, while samples C-4 h and C-8 h exhibited the optimal pore structure characteristics for m-xylene adsorption, they presented lower adsorption capacity compared to the 7HF-Vycor® carbon due to the electron withdrawing effect of the electronegative oxygen atom placed at the edges of the basal planes, which reduces the π-π interaction between the basal plane and the aromatic ring. On the other hand, introducing oxygen improves the electron density of the carbon framework, thus increasing its basicity, which in turn anchors the electron deficient carbon of the CO_2 to the pore surface by Lewis's acid-base interactions. So far, this explains the lower m-xylene and higher CO_2 adsorptivity of samples C-4 h and C-8 h as compared to the 7HF-Vycor® carbon.

However, the N-content of the carbons must be also considered and discussed to gain a more general view on the factors that affect the sample's adsorptivity. Hence, it is often reported that specific N groups such as pyridinic and amino groups contribute significantly to the low-pressure CO_2 and m-xylene adsorption, respectively. Theoretically, nitrogen being as much electronegative as oxygen should affect the CO_2 and m-xylene adsorptivity in a way like that of oxygen. However, the carbon from 7HF-Vycor® exhibits much higher N-content compared to C-4 h and C-8 h and this is in contrast to what reported above. It seems that the pore structural characteristics of the carbon samples define to a high extent whether the N-

doping will exert a profound effect on the CO_2 adsorption capacity. Explanatively, for the N-doping to have a positive impact on the CO_2 uptake, the linear CO_2 molecules must lie flat on the carbon surface, and this is favored in slit pore architectures rather than disordered carbon pore structures. Our samples, especially those derived with the templated precursor pathway like the carbon from 7HF-Vycor®, presented very complex pore structural characteristics and, consequently, N doping disclosed a marginal improvement on the CO_2 uptake.

Very recently, conjugated microporous polyanilines (CMPAs) have been developed via a facile approach that entails the use of simple salts to fine-tune the porosity and BET surface in a highly controllable way.[51–52] Apart from being highly effective adsorbents for CO_2 and heavy metals, this type of conjugated polymers, owing to the high abundance of N atoms in their structure, have been also applied as effective precursors for the development of N-autodoped hierarchical porous carbons (PTPACs) as very efficient CO_2 adsorbents that significantly surpass the adsorption capacity of their precursors.[53–54] Due to the low cost of their precursors as compared to ILs, the PTPACs carbons are highly competitive with the C-adsorbents developed in this work. For that reason, in Table 8 we present in comparison the CO_2 adsorption capacity of the relevant materials at almost identical conditions, based on the results available in the literature. The CO_2 adsorption capacity of the IL derived carbons outperforms that of the conjugated microporous polymers and may be slightly lower compared to that of PTPACs carbons considering that the results are obtained at higher temperature (25 °C instead of 0 °C) and at half relative pressure.

Conclusions

In this work, we have presented that templated IL pyrolysis and unconfined IL pyrolysis followed by activation with CO_2, brings to N-doped C-materials with different pore structural characteristics and pore surface properties. It has also been concluded that the pore size of the template, which in this work consisted of pore etched Vycor® with different degrees of pore etching, also affects the properties of the derived carbons.

The N-doped carbons produced with the templated IL pyrolysis method were tested as catalytic materials for the challenging electrochemical ORR. All materials exhibited remarkable efficiency in oxygen reduction with the sample produced from the template with the smaller pores being the most effective one. This was attributed to both the highly hierarchical pore structure and the higher surface area of this C-material, but also to the higher degree of N-doping achieved due to nanoconfinement of the IL precursor into smaller nanopores that strongly limits evaporative losses during pyrolysis.

As regards the adsorption capacity of the C-materials for m-xylene, this is primarily affected by the pore structural features with the most beneficial one being the existence of wide micropores with size centered around 20 Å. In addition, hierarchical pore structures entailing a large fraction of small mesopores have also a profound effect on the m-xylene adsorption capacity. It was also concluded that pyrolytic approaches that lead to a high population of oxygenated functional groups on the surface of the C-materials are not the best choice, when the target is to derive adsorbents for aromatic compounds. This is due to the electron withdrawing effect of the electronegative oxygen atom placed at the edges of the carbon basal planes, which reduces the π-π interaction between the basal plane and the aromatic ring. On the contrary, oxygenated groups are highly beneficial for CO_2 adsorption since their presence enhances the electron density (basicity) of the carbon framework that interacts strongly with the electron deficient carbon of CO_2.

Finally, while N-doping enhances the catalytic activity of the C-materials, it does not seem to have a significant effect on the CO_2 adsorptivity. The reason is that disordered pore structures, like that obtained with the templated IL approach, do not allow

Table 8. The CO_2 adsorption capacity of the N-doped carbons developed in this work, compared to that of conjugated microporous polymers and the respective N-doped carbons.

Source	Samples	Relative pressure (P/P_0)	T (°C)	CO_2 uptake (mmol/g)	Surface area (m^2/g)	Micropore volume (cm^3/g)	N content (%)
Carbons, this work	C-8 h	0.0155	25	1.60	229.2	0.119	12
	C-4 h	0.0155	25	1.25	148.8	0.086	10
	Carbon from 7HF-Vycor	0.0155	25	1.40	703.0	0.260	18
Conjugated microporous polymers[51]	PTAPA	0.0145	0	1.62	901	–	n/a
	PAPA	0.0145	0	1.75	1378	–	n/a
	CMP-1	0.0145	0	0.90	1148	0.800	n/a
	PTCT	0.0145	0	1.42	1263	0.730	n/a
	p-PPF	0.0145	0	0.50	215	0.065	n/a
Nitrogen-doped microporous carbons[54]	CMPA1-C1000	0.0290	0	4.70	977	0.64	1.6
	CMPA2-C1000	0.0290	0	4.20	292	0.24	2.1
	CMPA3-C1000	0.0290	0	5.10	800	0.57	2.1

for the linear CO_2 molecules to lie flat on the carbon surface, which is favored only in slit pore architectures.

Overall, this work exhibits that templated IL pyrolysis is an appropriate method for fabricating C-materials with hierarchical pore structure that can be used both as effective oxygen reduction reaction electrocatalysts and as adsorbents for aromatics, whereas the pyrolysis of unconfined IL followed by activation with CO_2 is more suitable for yielding microporous carbons with enhanced CO_2 adsorption capacity.

Acknowledgements

This research was partially funded by the European Union's Horizon Europe research and innovation programme within the KNOWSKITE-X project, under grant agreement No. 101091534.

In addition, the publication of the article in open access (OA) mode was financially supported by HEAL-Link.

Conflict of Interests

The authors declare no conflict of interest.

Data Availability Statement

The data that support the findings of this study are available from the corresponding author upon reasonable request.

Keywords: Ionic Liquids · N-doped carbon · electrocatalyst · adsorption · aromatics

[1] A. H. Lu, G.-P. Hao, X.-Q. Zhang in *Porous Materials for Carbon Dioxide Capture* (Eds.: A. H. Lu, S. Dai), Green Chemistry and Sustainable Technology, Berlin, Heidelberg, Springer, **2014**, pp. 15–77.
[2] A. B. Jorge, R. Jervis, A. P. Periasamy, M. Qiao, J. Feng, L. N. Tran, M.-M. Titirici, *Adv. Energy Mater.* **2020**, *10*, 1902494E.
[3] M.-M. Titirici, R. J. White, N. Brun, V. L. Budarin, D. S. Su F del Monte, J. H. Clark, M. J. MacLachlan, *Chem. Soc. Rev.* **2015**, *44*, 250–290.
[4] Y. Yang, K. Chiang, N. Burke, *Catal. Today* **2011**, *178*, 197–205.
[5] H. T. Gomes, B. F. Machado, A. Ribeiro, I. Moreira, M. Rosário, A. M. Silva, A. M. Figueiredo, J. L. Faria, *J. Hazard. Mater.* **2008**, *159*, 420–426.
[6] F. Hasché, M. Oezaslan, P. Strasser, *Phys. Chem. Chem. Phys.* **2010**, *12*, 15251–15258.
[7] E. Raymundo-Piñero, D. Cazorla-Amorós, A. Linares-Solano, *Carbon* **2003**, *41*, 1925–1932.
[8] D. Geng, Y. Chen, Y. Chen, Y. Li, R. Li, X. Sun, S. Ye, S. Knights, *Energy Environ. Sci.* **2011**, *4*, 760–764.
[9] D. S. Su, J. Zhang, B. Frank, A. Thomas, X. Wang, J. Paraknowitsch, R. Schlögl, *ChemSusChem* **2010**, *3*, 169–180.
[10] J. P. Paraknowitsch, A. Thomas, *Energy Environ. Sci.* **2013**, *6*, 2839–2855.
[11] P. L. Gai, O. Stephan, K. McGuire, A. M. Rao, M. S. Dresselhaus, G. Dresselhaus, C. Colliex, *J. Mater. Chem.* **2004**, *14*, 669–675.
[12] T. Lin, F. Huang, J. Liang, Y. Wang, *Energy Environ. Sci.* **2011**, *4*, 862–865.
[13] J. P. Paraknowitsch, Y. Zhang, B. Wienert, A. Thomas, *Chem. Commun.* **2013**, *49*, 1208–1210.
[14] S. Chalk, L. McEwen, *Chem. Int.* **2017**, *39*, 25–30.
[15] T.-P. Fellinger, A. Thomas, J. Yuan, M. Antonietti, *Adv. Mater.* **2013**, *25*, 5838–5855.
[16] J. P. Paraknowitsch, A. Thomas, M. Antonietti, *J. Mater. Chem.* **2010**, *20*, 6746–6758.
[17] W. N. W. Salleh, A. F. Ismail, T. Matsuura, M. S. Abdullah, *Sep. Purif. Rev.* **2011**, *40*, 261–311.
[18] N. Zou, X. Lin, M. Li, L. Li, C. Ye, J. Chen, T. Qiu, *ACS Sustainable Chem. Eng.* **2020**, *8*, 18054–18061.
[19] Z. Zhou, X. Chen, J. Worth, C. Ye, J. Chen, T. Qiu, *AIChE J.* **2023**, *69*, e18098.
[20] K. Xiao, Z. Zhou, C. Ye, J. Chen, T. Qiu, *Chem. Eng. J.* **2023**, *478*, 147398.
[21] M. Li, P. Lu, C. Ye, J. Chen, T. Qi, *Fuel* **2023**, *354*, 129269.
[22] M. E. Zakrzewska, E. Bogel-Łukasik, R. Bogel-Łukasik, *Energy Fuels* **2010**, *24*, 737–745.
[23] J. D. Holbrey, K. Seddon, *Ionic liquids. Clean products and processes* **1999**, *1*, 223–236.
[24] R. Sheldon, *Chem. Commun.* **2001**, 2399–2407.
[25] O. Tzialla, G. Kakosimos, C. Athanasekou, E. Galata, G. Romanos, G. Pilatos, L. Zubeir, M. Kroon, B. Iliev, T. Schubert, K. G. Beltsios, *Microporous Mesoporous Mater.* **2016**, *223*, 163–175.
[26] N. Sen, K. K. Singh, S. Mukhopadhyay, K. T. Shenoy, *Chem. Eng. Process.* **2021**, *166*, 108431.
[27] T. Ikeda, M. Boero, S.-F. Huang, K. Terakura, M. Oshima, J.-i. Ozaki, *J. Phys. Chem. C* **2008**, *112*, 14706–14709.
[28] G. Tuci, C. Zafferoni, A. Rossin, A. Milella, L. Luconi, M. Innocenti, L. Truong Phuoc, C. Duong-Viet, C. Pham-Huu, G. Giambastiani, *Chem. Mater.* **2014**, *26*, 3460–3470.
[29] B. Rubahamya, K. S. K. Reddy, A. A. Shoaibi, C. Srinivasakannan, *Fullerenes Nanotubes Carbon Nanostruct.* **2018**, *26*, 16–22.
[30] M. Mohamedali, D. Nath, H. Ibrahim, A. Henni, *Greenhouse Gases* **2016**, 115–154.
[31] F. Adib, A. Bagreev, T. J. Bandosz, *Langmuir* **2000**, *16*, 1980–1986.
[32] K. N. Marsh, J. A. Boxall, R. Lichtenthaler, *Fluid Phase Equilib.* **2004**, *219*, 93–98.
[33] T. Welton, *Chem. Rev.* **1999**, *99*, 2071–2084.
[34] J. S. Lee, X. Wang, H. Luo, G. A. Baker, S. Dai, *J. Am. Chem. Soc.* **2009**, *131*, 4596–4597.
[35] Y. Shao, J. Sui, G. Yin, Y. Gao, *Appl. Catal. B* **2008**, *79*, 89–99.
[36] I.D. Chapman, T.H. Elmer, *U.S. Patent 3,485,687*, **Dec. 1969**.
[37] J. Yuan, C. Giordano, M. Antonietti, *Chem. Mater.* **2010**, *22*, 5003–5012.
[38] P. Carrott, J. Nabais, M. R. Carrott, J. Pajares, *Carbon* **2001**, *39*, 1543–1555.
[39] G. Y. Gor, M. Thommes, K. A. Cychosz, A. V. Neimark, *Carbon* **2012**, *50*, 1583–1590.
[40] J. Benkhedda, J.-N. Jaubert, D. Barth, L. Perrin, M. Bailly, *The J. Chem. Thermodynamics* **2000**, *32*, 401–411.
[41] M. M. Abdel daiem, J. Rivera-Utrilla, M. Sánchez-Polo, R. Ocampo-Pérez, *Sci. Total Environ.* **2015**, *537*, 335–342.
[42] J. D. Méndez-Díaz, M. M. Abdel daiem, J. Rivera-Utrilla, M. Sánchez-Polo, I. Bautista-Toledo, *J. Colloid Interface Sci.* **2012**, *369*, 358–365.
[43] I. Velo-Gala, J. J. López-Peñalver, M. Sánchez-Polo, J. Rivera-Utrilla, *Carbon* **2014**, *67*, 288–299.
[44] J. Chen, J. Yang, G. Hu, X. Hu, Z. Li, S. Shen, M. Radosz, M. Fan, *ACS Sustainable Chem. Eng.* **2016**, *4*, 1439–1445.
[45] M. Peyravi, *Polym. Adv. Technol.* **2018**, *29*, 319–328.
[46] M. Wang, X. Fan, L. Zhang, J. Liu, B. Wang, R. Cheng, M. Li, J. Tian, J. Shi, *Nanoscale* **2017**, *9*, 17593–17600.
[47] Y. Wang, X. Hu, T. Guo, J. Hao, C. Si, Q. Guo, *Front. Chem. Science Eng.* **2021**, *15*, 493–504.
[48] C. D. Baertsch, H. H. Funke, J. L. Falconer, R. D. Noble, *J. Phys. Chem.* **1996**, *100*, 7676–7679.
[49] C.-M. Wang, K.-S. Chang, T.-W. Chung, H. Wu, *J. Chem. Eng. Data* **2004**, *49*, 527–531.
[50] F. Janvier, L. Tuduri, D. Cossement, D. Drolet, J. Lara, *Carbon* **2015**, *94*, 781–791.
[51] J. Chen, T. Qiu, W. Yan, C. F. J. Faul, *J. Mater. Chem. A* **2020**, *8*, 22657–22665.
[52] J. Chen, W. Yan, E. J. Townsend, J. Feng, L. Pan, V. D. A. Hernandez, C. F. J. Faul, *Angew. Chem. Int. Ed.* **2019**, *58*, 11715–11719.
[53] X. Lou, X. Chen, D. Tang, Q. Wang, Y. Tian, M. Tu, Y. Wang, C. Ye, J. Chen, T. Qiu, *Langmuir* **2022**, *38*, 13238–13247.
[54] D. Tang, X. Lyu, Z. Huang, R. Xu, J. Chen, T. Qiu, *Powder Technol.* **2023**, *427*, 118769.

Manuscript received: December 29, 2023
Revised manuscript received: March 4, 2024
Accepted manuscript online: March 4, 2024
Version of record online: March 21, 2024